Cardiovascular Engineering and Technology (2024) 15:647–666
https://doi.org/10.1007/s13239-024-00741-2

BMES BIOMEDICAL ENGINEERING SOCIETY

REVIEW

A Pseudo-Spectral Method for Wall Shear Stress Estimation from Doppler Ultrasound Imaging in Coronary Arteries

Jimena Martín Tempestti[1] · **Saeyoung Kim**[2,3] · **Brooks D. Lindsey**[2,3,4] · **Alessandro Veneziani**[1,5]

Received: 18 September 2023 / Accepted: 24 June 2024 / Published online: 5 August 2024

Abstract

Purpose The Wall Shear Stress (WSS) is the component tangential to the boundary of the normal stress tensor in an incompressible fluid, and it has been recognized as a quantity of primary importance in predicting possible adverse events in cardiovascular diseases, in general, and in coronary diseases, in particular. The quantification of the WSS in patient-specific settings can be achieved by performing a Computational Fluid Dynamics (CFD) analysis based on patient geometry, or it can be retrieved by a numerical approximation based on blood flow velocity data, e.g., ultrasound (US) Doppler measurements. This paper presents a novel method for WSS quantification from 2D vector Doppler measurements.

Methods Images were obtained through unfocused plane waves and transverse oscillation to acquire both in-plane velocity components. These velocity components were processed using pseudo-spectral differentiation techniques based on Fourier approximations of the derivatives to compute the WSS.

Results Our Pseudo-Spectral Method (PSM) is tested in two vessel phantoms, straight and stenotic, where a steady flow of 15 mL/min is applied. The method is successfully validated against CFD simulations and compared against current techniques based on the assumption of a parabolic velocity profile. The PSM accurately detected Wall Shear Stress (WSS) variations in geometries differing from straight cylinders, and is less sensitive to measurement noise. In particular, when using synthetic data (noise free, e.g., generated by CFD) on cylindrical geometries, the Poiseuille-based methods and PSM have comparable accuracy; on the contrary, when using the data retrieved from US measures, the average error of the WSS obtained with the PSM turned out to be 3 to 9 times smaller than that obtained by state-of-the-art methods.

Conclusion The pseudo-spectral approach allows controlling the approximation errors in the presence of noisy data. This gives a more accurate alternative to the present standard and a less computationally expensive choice compared to CFD, which also requires high-quality data to reconstruct the vessel geometry.

Keywords Wall shear stress · Doppler imaging · Interpolation · Numerical differentiation · Computational fluid dynamics

---

Associate Editor Zhenglun Alan Wei oversaw review of this article.

Jimena Martín Tempestti and Saeyoung Kim have contributed equally to this work.

✉ Jimena Martín Tempestti
jimena.martin@emory.edu

Saeyoung Kim
sykim@gatech.edu

Brooks D. Lindsey
brooks.lindsey@bme.gatech.edu

Alessandro Veneziani
avenez2@emory.edu

[1] Department of Mathematics, Emory University, 400 Dowman Dr, Atlanta 30322, GA, USA

[2] George W. Woodruff School of Mechanical Engineering, Georgia Institute of Technology, 801 Ferst Dr., Atlanta, GA 30332, USA

[3] Interdisciplinary BioEngineering Graduate Program, Georgia Institute of Technology, 315 Ferst Dr., Atlanta, GA 30332, USA

[4] Wallace H. Coulter Department of Biomedical Engineering, Georgia Institute of Technology and Emory University, 313 Ferst Dr NW, Atlanta, GA 30332, USA

[5] Department of Computer Science, Emory University, 400 Dowman Dr, Atlanta, GA 30322, USA

Introduction

Wall shear stress (WSS) has been shown to trigger a change in endothelial cells' behaviors and is considered important in the development of atherosclerosis in coronary arteries [1, 2]. Coronary segments with low WSS are linked with greater plaque progression and constrictive vascular remodeling while segments with high WSS are associated with increased plaque vulnerability by expansive arterial remodeling [3–9].

A direct measurement of WSS is not possible, so Computational Fluid Dynamics (CFD) is used to solve the Navier–Stokes equations - describing the blood flow - in reconstructed anatomical models from patient-specific Computed Tomography (CT) angiography or Magnetic Resonance Imaging (MRI) images [10]. The solution to the Navier–Stokes equations provides complete velocity and pressure information at any location in the coronary artery. The outcome of CFD heavily relies on the quality of the input data such as reconstructed vessel geometry and proper boundary conditions, so it is crucial to acquire accurate input information [11, 12]. Also, CFD analyses can be time-consuming.

Since WSS can be computed from the gradient of velocity field distributions and blood viscosity, other researchers have used phase contrast MRI (PC-MRI) to measure the velocity and then to estimate the WSS. For instance, Oyre et al. estimated the WSS in a common carotid artery by least-square fitting a three-dimensional paraboloid to the velocity data. Next, the WSS was obtained by differentiating the velocity quadratic functions and multiplying the velocity gradient at the vessel wall by the dynamic blood viscosity [13–15]. Since this method assumes parabolic velocity flow profiles and does not consider non-radial components of the velocity gradient, interpolation based on piece-wise cubic Lagrangian basis functions was successively used to further improve the fitting of the velocity profiles [16–18]. However, because of the low spatial resolution, WSS estimation using PC-MRI has currently been limited to larger blood vessels such as a carotid artery, carotid bifurcations, or abdominal aorta [11, 16, 19, 20].

Recently, ultrasound-based minimally invasive intravascular velocity measurement devices have been developed to image smaller arteries such as coronaries [21–24]. In the future, intravascular ultrasound imaging devices may potentially be used to derive WSS from direct velocity measurements in coronary arteries.

The most straightforward way to estimate WSS using ultrasound (US) Doppler velocimetry is to measure only the peak velocity and estimate mean WSS from the standard Poiseuille-Hagen solution under the assumption of the fully developed and parabolic flow profile and the vessel being axisymmetric [25, 26]. However, in situations where the flow profile is not parabolic, this approach results in a large error (maximum 55%) in WSS estimation [25, 27, 28].

To avoid this problem, recent developments in ultrasound Doppler velocimetry have combined plane wave transmission with transverse oscillation techniques to estimate 2D vector velocity at a higher spatial and temporal resolution, thus for the estimation of WSS, local flow velocity measurements near the wall are possible [29–32]. Wang et al. estimated WSS in a human femoral artery from the tangential stress tensor vector and used the rotation matrix to align the tensors to the wall curvature, but have not validated this approach with other imaging modalities [33]. Furthermore, to account for both contributions from axial and lateral velocities, Chee et al. used both components to calculate the WSS in carotid artery bifurcation [34]. The performance of this approach was compared only to reference values computed from CFD in simple geometries and flow conditions. In Ref. [35], the authors propose a method based on 2D US measure, based on the assumption of a Poiseuille profile projected along the tangential direction. The velocity is differentiated by a finite difference procedure, evaluating the velocity data in different positions and then retaining either the average or the maximum to mitigate the impact of the noise.

Another method for estimating local 2D velocity vector and WSS using ultrasound is echo-Particle Image Velocimetry (PIV). Echo-PIV tracks contrast agent microbubbles in flow by cross-correlating consecutive ultrasound B-mode images. Using echo-PIV approach, the entire estimated velocity profile was filtered and fitted using polynomial fit, and WSS was calculated from the fitted velocity profile by computing its gradient at the vessel wall in larger arteries such as the aorta, brachial artery, or carotid bifurcation [25, 36–40]. Because in complex geometry, the general shape is not known, a fit through only a few points near the wall was instead used to estimate WSS [41]. However, these WSS estimation approaches have not been validated against CFD or other imaging modalities, nor have they been validated in more complex geometries such as stenotic vessels.

The purpose of the present work is to introduce a new method to calculate WSS using as input the ultrasound velocity, where two "in-plane" velocity components (axial and lateral) are available at a given section. Thus this method is tailored for 2D velocity data without the need for assuming flow profiles or relying on anatomical geometries derived from imaging. The method is based on a Fourier approximation of the velocity data as opposed to polynomial fitting. This approximation of the velocity and its gradient (generally referred to as the *pseudo-spectral derivative*) controls the numerical errors, particularly in the presence of high-frequency noise. We also incorporate the lateral velocity

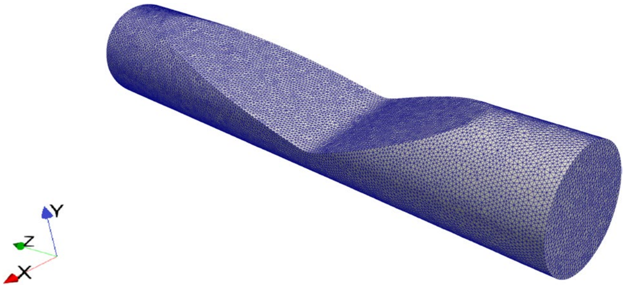

Fig. 1 Geometry and surface mesh of the stenotic vessel considered in the present work

component available from 2D vector Doppler ultrasound imaging and the shape of the wall in the WSS computation.

Our method is compared against methods based on the Poiseuille-Hagen solution [25, 26, 35], and CFD simulations. Both non-stenotic and stenotic vessels were tested. CFD is used as the validation tool because it is largely considered the best reference standard for obtaining WSS [19]. We tested our method against synthetic measures extracted from CFD that mimic the ultrasound data extraction to probe the estimation in an ideal "noise-free" situation, assuming that numerical errors in the CFD are generally much smaller than measurement errors (as is the case for a fine mesh). Finally, WSS results estimated from US imaging were compared with the Poiseuille-based WSS estimation methods. The results show that, in the absence of noise, all the methods can provide an excellent evaluation of the WSS, with numerical errors comparable with the CFD estimation. However, in the presence of noise coming from a real measurement campaign, the PSM is superior for its natural low-pass filtering nature, leading to very good clinical accuracy.

The ultimate purpose of this research is to implement our method in a forward-viewing intravascular ultrasound transducer to enable plaque vulnerability characterization inside the coronary arteries for stratifying risks. A more extended presentation of the results of our method in experimental *ex vivo* settings that mimic stenotic vessels is reported in Ref. [42].

Materials and Methods

US Experimental Setup

Two geometries of vessels with a length of 12 mm and a diameter of 3.2 mm to mimic the physiological and pathophysiological conditions in coronary arteries were prepared: a straight vessel with eccentric stenosis of 54% diameter stenosis (% DS) displayed in Fig. 1 and a straight vessel without stenosis as the control case. This diameter of vessel was selected because it corresponds to the diameter of a healthy human left anterior descending (LAD) coronary artery [43], and this value of % DS is in the range of intermediate severity of LAD (40–70%) [44], and this severity of stenosis presents challenges to clinicians when stratifying risk for patients with stable coronary artery [45, 46]. These geometries were first created in Solidworks [47] and 3D printed using a high-resolution StereoLithography Apparatus (SLA) resin printer (FormsLabs Form 3+) with a layer thickness of 25 µm. The printed geometries were placed on a phantom container, and a tissue-mimicking material (7.5% gelatin, 2% graphite as scattering particles, and 5% n-propanol) was poured around [48]. When the material had set, 3D-printed coronary geometries were removed, leaving an arterial lumen inside the phantom.

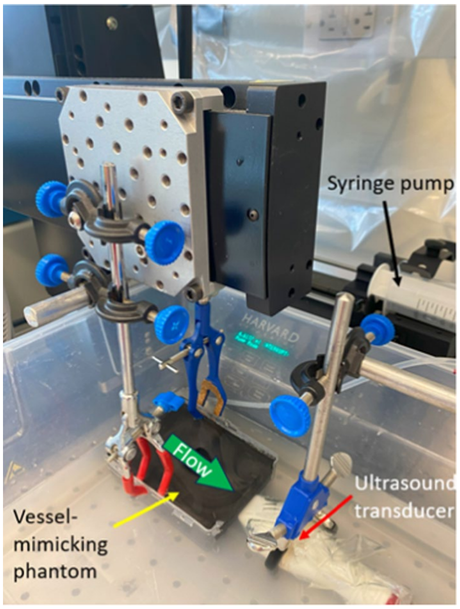

Fig. 2 Experimental setup. Flow is introduced into the vessel-mimicking phantom using the syringe pump and the flow is directed towards the linear array ultrasound transducer which is placed at the outlet of the phantom. The ultrasound transducer is connected to a high frame rate ultrasound imaging system

Each phantom was placed inside a tank filled with degassed water. A high-frequency linear array transducer (VisualSonics MS400, FUJIFILM VisualSonics, Inc., Toronto, Canada) was placed 1 mm from the outlet of the phantom vessel. The transducer's beam was facing toward the flow, and the flow was introduced toward the transducer using a syringe pump (PHD 2000, Harvard Apparatus, Holliston, MA). The continuous and steady flow had a 15 mL/min flow rate. This time-averaged velocity corresponds to the mean physiological flow rates and velocities found in LAD coronary arteries in adults [49, 50] (Fig. 2).

While the data sets in these studies were acquired using a high-frequency linear array (Visualsonics MS 400), in vivo data will require a forward-viewing, 20 MHz 2D

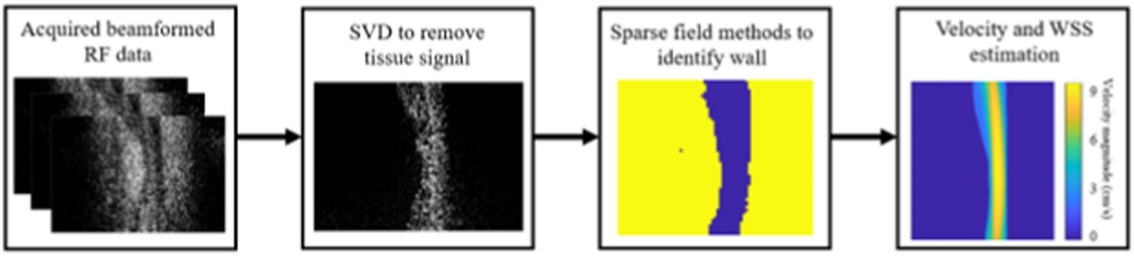

Fig. 3 Diagram showing the ultrasound image segmentation and processing. RF refers to Radio Frequency, SVD stands for Singular Value Decomposition, and WSS represents Wall Shear Stress

intravascular ultrasound array, which we are currently building. Due to the decreased aperture size of the intravascular array and the ability to position the intravascular array closer to the region of interest in the artery, the spatial resolution is approximately a factor of six worse according to simulations [24]. Briefly, simulations of ultrasound imaging of blood flow in a straight vessel at the same velocity used in the presented studies indicate that spatial averaging due to increased size of the point spread function results in an overestimation of approximately 11% when using the intravascular array, however, estimation error for other velocities and flow rates have not yet been investigated [24].

US Imaging and Vector Doppler Velocity Estimation

An accurate velocity profile is needed to estimate WSS using ultrasound data. In this project, a Doppler approach was adopted, where images were obtained through unfocused plane waves and transverse oscillation (to acquire both in-plane velocity components). The linear array transducer was connected to a high frame rate ultrasound imaging system (Verasonics Vantage 256, Kirkland, WA, USA). To acquire beamformed Radio Frequency (RF) data, unfocused plane waves at a frequency of 23MHz were selected, employing 3-angle compounding ($-15°, 0°, 15°$). The data was obtained at a frame rate of 8,000 frames per second. In total, 200 frames were acquired, and the transmitting signals were set with a two-pulse duration cycle. For each phantom, a series of five data sets were collected. The segmentation process is summarized in Fig. 3.

Post-processing was performed in MATLAB [51]. First, the stationary phantom backgrounds were eliminated by employing Singular Value Decomposition (SVD) to remove the first, largest singular vector [52]. Next, to estimate the lateral velocity, we introduced transverse oscillation by applying a Gaussian filter centered around the desired lateral oscillation frequency to the data in the Fourier domain [31, 53]. In particular, we adopted a wavelength λ_x and a bandwidth σ_x equal to 0.0613 mm. Finally, to estimate the lateral velocity component, a fourth-order autocorrelation estimator was utilized. As for the axial velocity component, a standard cross-correlation estimator was employed. An ensemble size of 200 was used, and the position of the wall was determined using a sparse field method with a mask excluding the area outside the vessel [39, 54]. Based on this approach, the pixels containing the wall were set to zero velocity so that only the velocity values from Doppler data inside the wall were used. For more details on ultrasound acquisition see [55].

Mathematical Modeling

The dynamic of an incompressible fluid with velocity $\boldsymbol{u}$ and pressure p in a region of interest Ω is described by the incompressible Navier–Stokes equations

$$\begin{cases} \rho\frac{\partial u}{\partial t} + \rho(\boldsymbol{u}\cdot\nabla)\boldsymbol{u} + \nabla\cdot\boldsymbol{\sigma} + \nabla p = 0 \\ \nabla\cdot\mathbf{u} = 0 \end{cases} \tag{1}$$

obtained by applying the conservation of momentum and mass. Here ρ denotes the (constant) blood density and, for a Newtonian fluid, the deviatoric stress tensor reads

$$\boldsymbol{\sigma} = -\mu\left(\nabla\boldsymbol{u} + \nabla^T\boldsymbol{u}\right) \tag{2}$$

where μ is the (positive) constant kinetic viscosity. In this study, for our CFD testing, we will consider steady cases, i.e. the solution of

$$\begin{cases} \rho(\boldsymbol{u}\cdot\nabla)\boldsymbol{u} + \nabla\cdot\boldsymbol{\sigma} + \nabla p = 0 \\ \nabla\cdot\mathbf{u} = 0. \end{cases} \tag{3}$$

The Wall Shear Stress (WSS) on a portion of the boundary $\Gamma \subset \partial\Omega$ is defined as the part of the normal component of the deviatoric tensor $\boldsymbol{\sigma}\cdot\boldsymbol{n}$ tangential to the boundary (here $\boldsymbol{n}$ is the outward normal unit vector), and can be defined as

$$\boldsymbol{\tau} \equiv \boldsymbol{\sigma}\cdot\boldsymbol{n} - (\boldsymbol{n}\cdot\boldsymbol{\sigma}\cdot\boldsymbol{n})\boldsymbol{n}. \tag{4}$$

To compute the WSS, one can either solve the Eq. (1), or measure the velocity $\boldsymbol{u}$ and then apply (2, 4). In general, Eq. (1) cannot be solved analytically, CFD is required. However, in some special cases, we have the analytical solution, like for a flow in a rectilinear, circular cylindrical domain under a given pressure drop either constant in time (Poiseuille or

Poiseuille-Hagen solution) or periodic in time (Womersley solution) [56]. Assuming that the cylinder axis is along the Cartesian x_3-axis, the Poiseuille-Hagen solution reads

$$u_1 = u_2 = 0, \quad u_3 = \frac{u_{max}}{R^2}\left(R^2 - x_1^2 - x_2^2\right) \tag{5}$$

where the index 1 refers to the velocity component along x_1 (2 and 3 along the x_2 and x_3 directions respectively[1]), R is the radius of the cylinder (where the velocity is zero by virtue of non-slip conditions) and u_{max} is the axial velocity function of the prescribed pressure drop. In this particular case, the WSS reads

$$\boldsymbol{\tau}_P \equiv \mu \frac{\partial u_3}{\partial r} = -2\mu \frac{u_{max}}{R} \tag{6}$$

where $r \equiv \sqrt{x_1^2 + x_2^2}$ is the radial coordinate.

Adopting $\boldsymbol{\tau}_P$ to calculate the WSS of a generic flow supposedly introduces a significant approximation of the real value WSS, as lateral velocity components are neglected, as well as the wall shape. This approximation has been traditionally adopted to estimate WSS from velocity measurements, and $\frac{\partial u_3}{\partial r}$ has been obtained by interpolating a quadratic (or cubic) function to three (or four) points closest to the wall where velocity was measured. The derivative in the radial direction is calculated analytically from the interpolated function [41]. Generally, the radial direction is approximated with one of the cartesian ones. In this work, this approach will be identified as the *Poiseuille method*.

In the study [35] mentioned above, the significance of considering the radial component in WSS estimation was demonstrated. Their method involves isolating the tangential velocity component relevant to WSS by utilizing the dot product of velocity components with a tangential unit vector. The velocity rate of change is computed with a Finite Difference (FD) approach at multiple points near the vessel wall and then either selecting the maximum value or computing an average. Both the strategies aim at mitigating the presence of noise in the data and the approximation induced by the assumption of a Poiseuille profile.

In contrast, our approach considers both radial and tangential velocity components as well as the vessel's shape in Eq. (4) that inherently integrates these factors. Additionally, we depart from the finite difference approach used by Ref. [35], instead opting for a pseudo-spectral interpolation technique. This method not only facilitates WSS calculation but also effectively denoises the data, marking a significant innovation in our approach. While our measures here are 2D in-plane velocities, it is worth noting that our methodology, based on (4) and not (6) can be promptly extended to 3D data sets. This will be a follow-up of the present work, that is expected to increase the accuracy of the WSS estimates in real geometries with significant out-of-plane velocity components.

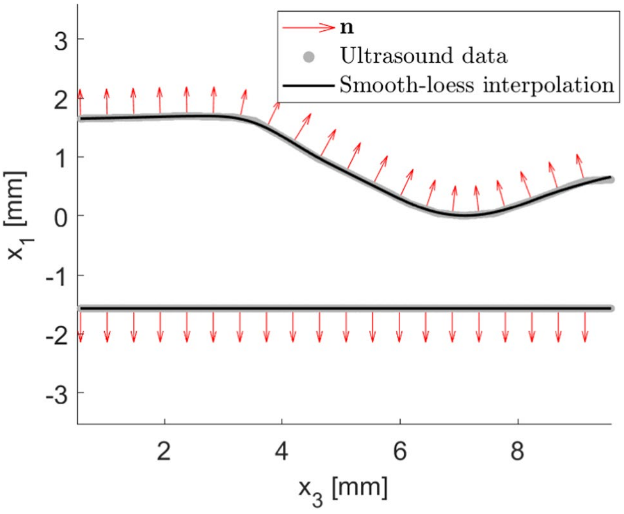

Fig. 4 In-plane boundary detection and Smooth-Loess MATLAB interpolation on the profile of the stenotic vessel considered in the present study. Here, ***n*** represents the outward normal unit vector to the vessel wall

Boundary Extraction and Fitting

As stated in "US Imaging and Vector Doppler Velocity Estimation" Sect., our velocity measures provide two in-plane velocity components that we denote as *lateral* (u_1) and *axial* (u_3). Data are expressed as point-wise measures of velocity in the image pixels, with an 8.3-μm resolution. This is the distance between two pixels, i.e., two different measures of velocity. We will call this distance h.

Assuming no-slip conditions on the boundary, the vessel wall was detected by the zero-velocity pixels. The identification of these points provides a pixelized boundary with artificial discontinuities that prevent the calculation of an accurate continuous normal vector and ultimately a straightforward use of Eq. (4). We need, therefore, to use the points to fit a regular curve to describe the boundary. The classical LOESS (LOcally Estimated Scatterplot Smoothing) method implements a local regression using weighted linear least squares [57]. In particular, here we used the MATLAB built-in function *smooth* with the option *Loess* [51]. We use polynomials of order 2, with a 30%-data span (i.e., 30% of the total data set was used to fit each local polynomial).

Figure 4 shows the boundary obtained for the profile of the stenotic vessel from the US imaging (grey dots), the interpolated smooth-Loess functions for the bottom- and

---

[1] We opt for the notation x_1, x_2, x_3 for x, y and z respectively, for the sake of easiness of writing/reading the mathematical equations.

top-vessel walls (solid black lines), and corresponding normal vectors (computed by differentiation) at different locations (red arrows). Differences between discrete data and interpolated function are almost imperceptible; nonetheless, the latter provides a continuous and smooth first derivative.

Data Fitting and Numerical Differentiation

To compute the deviatoric stress tensor $\boldsymbol{\sigma}$ one needs to calculate the velocity gradient $\nabla \boldsymbol{u}$ with components $\partial u_i / \partial x_j$, $i, j = 1, 2, 3$.

However, US imaging provides only in-plane velocities. As mentioned earlier, the image plane is spanned by the (x_1, x_3) coordinates, so only u_1 and u_3 are available. Correspondingly, the available velocity gradient reduces to the 2×2 tensor with entries $\partial u_i / \partial x_j$ with $i, j = 1, 3$.

A possible approach for the computation of the derivatives consists of performing a polynomial interpolation of the velocity data close to the detected boundary and then differentiating the polynomial on the boundary. In the case of the Poiseuille approach, assuming that the radial direction coincides with the lateral one x_1, one can compute the quadratic polynomial interpolating the three velocity data close to the boundary and then differentiate the polynomial on the point closest to the boundary. Alternatively, a cubic polynomial can be computed, including the point detected on the boundary in the interpolation, where the velocity data, by definition, are null.

The derivative required is trivially the derivative of the quadratic or the cubic function in the two cases, respectively. Notwithstanding its simplicity, this approach guarantees accurate results for a small spatial resolution h when the velocity data are accurate. In the presence of noise, the differentiation increments the impact of the noise with a factor h^{-1} (h is of the order of a few microns). See the discussion in Appendix, inequality (12).

It is worth stressing that the binary discrete definition of the boundary causes some loss of information at the location where derivatives need to be calculated. For the sake of exemplification, Fig. 5 shows two velocity profiles for u_3 from the phantom vessel described in "US Experimental Setup" Sect., at 2.0 and 6.5 mm along the x_3-axis, respectively. The velocity profiles are embedded in a longer segment spanning the in-plane data measured by the ultrasound. The boundary of the vessel is represented by the end points of the portion of the segment where the data are non-zero (the so-called "support"). The black circles represent the data. The inaccuracies of the identification of the boundary exactly where the derivative needs to be computed are apparent. This adds additional perturbation to the derivative evaluation.

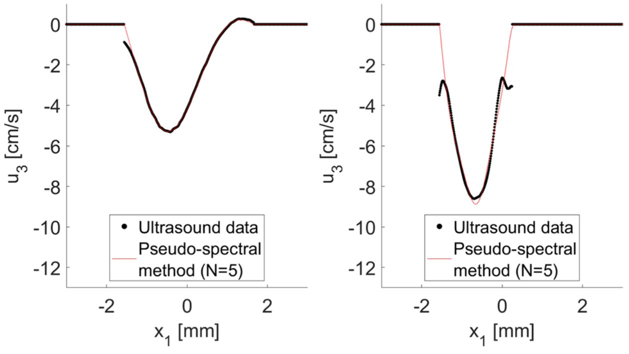

(a) (b)

Fig. 5 Axial velocity profiles (u_3) obtained from ultrasound imaging (circle makers) and their representation using a truncated Fourier Sine Series at five terms (red curve, $N = 5$): **a** at position $x_3 = 2.0mm$, **b** at position $x_3 = 6.5mm$

Pseudo-Spectral Radial Derivatives The pseudo-spectral approach we pursue here consists of computing a regular function from the available data as a Fourier sum.

A regular function $f(x)$ defined on a bounded interval $[a, b]$ can be represented by a sine Fourier series (see e.g. [58]) $f(x) = \sum_{j=1}^{\infty} c_j \psi_j(x)$ with

$$\psi_j(x) = \sin\left(\frac{j\pi}{b-a}(x-a)\right),$$
$$c_j = \frac{\int_a^b f \psi_j dx}{\int_a^b \psi_j^2 dx} = \frac{2}{b-a} \int_a^b f \psi_j dx. \tag{7}$$

If we replace the series with its truncation to the term N, we obtain an approximation of f with

$$f_N(x) \equiv \sum_{j=1}^{N} c_j \psi_j(x). \tag{8}$$

These formulas stem from regarding $f(x)$ in $[a, b]$ as the portion of a periodic function on the real axis, odd on a period (that leads to a sine-only series).

This approximation is *optimal*, in the sense that in the subspace of sinusoidal functions with maximum frequency N, it is the best approximation of f (i.e., the error $f - f_N$ is orthogonal to f_N). As recalled in the Appendix, the decay of the approximation error, particularly for regular functions, is fast with N (larger is N and smaller is the error). For regular functions, high accuracy is also obtained when we approximate f' with f'_N (see the Appendix).

However, in practice, this approach (called "spectral derivative") is not possible as the integrals for the coefficients c_j requires the knowledge of $f(x)$ while we have only the measures of f in the pixels. For this reason, we resort to a discrete version of the Fourier approximation where the integrals are replaced by quadrature formulas (such as the trapezoidal rule) having the available data as quadrature points. In this way,

$$\int_a^b f\psi_j dx \approx \sum f(x_q)\psi_j(x_q)w_q \tag{9}$$

where x_q are the points where the measures are available, and w_q are the quadrature weights. This well-known approach goes under the name of Discrete Fourier Transform (DFT) [58].

Once the velocity profiles u_1 and u_3 are DFT approximated as a function of x_1 for each value of the axial coordinate x_3, we can estimate their derivatives along x_1 by the analytical differentiation:

$$\frac{\partial u_i}{\partial x_1} \approx \sum_{j=1}^{N} \hat{c}_j(u_i)\frac{\partial \psi_j}{\partial x_1}, \quad i = 1,3 \tag{10}$$

where $\hat{c}_j$ are the Fourier coefficients computed by the DFT. As we recall in the Appendix, the accuracy of the derivative of the approximant computed with this approach ("pseudo-spectral differentiation") is very high for regular functions.

In practice, we can use this approach for the velocity data in two ways,

1. on the entire data set retrieved in-plane in the rectangular domain (*extended approach*), including the zero-velocity points that do not correspond to physical points in the domain of interest (i.e., externally to the support); in this case, a and b are the limits of the plane of the data;
2. on the support, i.e., the portion where the profile is not null (*restricted approach*), closed by the two endpoints, i.e., the first pixels where the velocity is zero; in this case, a and b are those endpoints.

The restricted approach works on a smaller data set. The sine Fourier expansion relies on the periodic odd extension of this function with better regularity properties to avoid the Gibbs phenomenon [59]. Therefore, we opted for this latter approach.

It is reasonable to assume that the measured velocity is composed of a signal and a noise (see the Appendix). Assuming that the noise v is purely random, in the absence of systematic errors in the measurement devices, the spectrum of v has a minimal contribution at the low frequencies, so the Fourier coefficients of the noise are generally small for low values of j. Based on these considerations, not only the Fourier truncation is an optimal approximation, but with an appropriate selection of the truncation index N, it may provide a low-pass approximation quite insensitive to the noise. These arguments will be tested in our Results section.

Axial derivatives

Approximating u_1 and u_3 along the axial coordinate x_3 is not trivial because the boundary of the vessel is not aligned along the axial coordinate (unless we are in a circular cylindrical domain). For this reason, an accurate pseudospectral fitting along the axial direction is problematic. Assuming that the axial derivatives have a minor impact on the WSS (we will discuss this point later), we opted for a finite difference approach after a suitable regularization of the data for the sake of denoising. A moving average smoothing was applied along x_3 with a 3%-data span, i.e., each smoothed value corresponds to the average of neighbor data points, and the length of the averaging interval is 3% of the total data set.

A classical finite difference approach reads

$$\frac{\partial u_i}{\partial x_3}(\bar{x}_1, \bar{x}_3) \approx \frac{u_i(\bar{x}_1, \bar{x}_3 + h) - u_i(\bar{x}_1, \bar{x}_3)}{h}, \quad i = 1,3$$

and it was applied by selecting pair of points $(\bar{x}_1, \bar{x}_3)$ and $(\bar{x}_1, \bar{x}_3 + h)$ close to the boundary. Since the boundary is, in general, a nontrivial function of x_3, the choice of these points follows the profile in a way such that they are always inside the vessel, so to rely on the available measures.

CFD solver

For the computation of the fluid in the domains of interest to provide a reference solution for the WSS, we wrote a Python code based on the Finite Element Library Fenics [60]. The solver uses inf-sup compatible Taylor-Hood finite elements $P^2 - P^1$ and a classical Newton linearization for the numerical treatment of the nonlinear term. Simulations are run under the steady regime with inflow boundary conditions specifying a flow rate through the prescription of a parabolic profile, while traction-free conditions are prescribed at the outflow. The WSS is computed by projecting the derivatives on a piecewise constant discontinuous Galerkin space, as described in Ref. [60].

The code is available upon request to the authors.

Results

To test our method in practice, we consider two geometries,

1. a cylindrical circular domain (Poiseuille-Hagen flow);
2. the stenotic geometry described in "Materials and Methods" Sect.—see Fig. 1.

In both cases, we assume a steady flow. For the comparative purpose of the present work, steady flow is an excellent test.

For clinical purposes, we will consider unsteady conditions in the follow-up of the present work. In the former case, we validate our results against (a) the analytical solution (6) and (b) the Poiseuille method (using a quadratic interpolation is exact in this case). As data to construct the WSS pseudo-spectral approximation, we used both the analytical velocity and the velocity obtained by CFD results, which we may consider as data added by numerical errors playing the role of noise.

In the stenotic case, the results of our method are compared against (a) the solution computed by the CFD simulations; (b) the Poiseuille method. The CFD-computed WSS is considered in this case as the ground truth in the absence of analytical solutions. We performed two tests: in the first one, we used the CFD velocity as the source of data to be used for both the Poiseuille and the pseudo-spectral WSS estimation. In the second case, we used the real measures obtained by the US, as described in "Materials and Methods" Sect. In this case, we also compared our results against the method proposed in [35] based on a FD approximation of the radial derivative of the tangential velocity.

In order to reduce the numerical errors amplified by the differentiation, in this stenotic case, results obtained by the Poiseuille method were post-processed with a 25-point moving average smoothing.

Poiseuille Flow

We consider the Poiseuille flow in a pipe with radius $R = 1.632mm$ (a value similar to the one for the stenotic case presented afterward), water viscosity $\mu = 0.01g/(cm \cdot s)$, and unit velocity at the center of the pipe of $u_{max} = 1cm/s$. Hence, Eq. (6) gives the constant benchmark value of WSS= $-0.0123Pa$ along the axis of the pipe.

Computational Fluid Dynamics

The Poiseuille flow case with a known analytical solution is used to validate our CFD solver. The simulation error was evaluated using two metrics on the WSS estimation: (1) the L^2-norm, and (2) the average difference (aka L^1-norm).

The cylindrical domain (Fig. 6a) was represented by an increasing number of linear tetrahedral elements, and after imposing the Poiseuille flow boundary conditions, a parabolic flow distribution was obtained at each time (Fig. 6b). The accuracy of the simulation was evaluated on the WSS estimation, and in particular, the convergence towards the analytical solution was studied with respect to the maximum mesh edge length H (Fig. 6c and Table 1). In this particular case, the discretization error for the finite element approximation of the Navier–Stokes equations is null because the solution belongs to the same finite dimensional space of the numerical approximation (quadratic for the velocity and linear for the pressure). The source of error comes from the geometrical approximation of the cylinder with a mesh of linear tetrahedra. The error on the velocity and the pressure is quadratic with the mesh size [61]. The expected error for the derivative of the velocity is, therefore, linear in L^2 with the mesh size H (see [58]). This linear behavior is confirmed in the Table 1, see also Fig. 6c. It is important to stress that this is not a mesh-independence study: here we are just probing the consistency between the convergence theory and our numerical results, so we are comparing the solutions with different meshes with the exact solution. A mesh-independence study is carried out later.

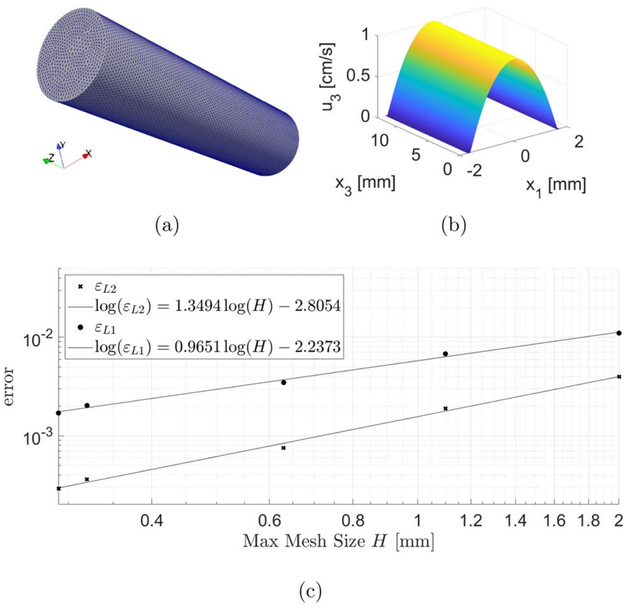

(a) (b)

(c)

Fig. 6 Simulation of Poisseuille flow using CFD: **a** Mesh; **b** Numerical solution of the velocity field, **c** CFD convergence computation, where, the simulation error was evaluated using two metrics on the WSS estimation: (1) the L^2-norm ε_{L2}, and (2) the average difference ε_{L1}

Table 1 Converge study based on two WSS estimation metrics: (1) the L^2-norm ε_{L2}, and (2) the average difference ε_{L1}

H [mm]	ε_{L2}	ε_{L1}
0.200	0.01104	0.00399
0.110	0.00680	0.00189
0.063	0.00347	0.00075
0.032	0.00203	0.00036
0.029	0.00170	0.00029

WSS Estimation

From the CFD numerical solution, it is possible to extract velocity values in a rectangular regular grid in a setting analogous to the one available from ultrasound imaging. Then,

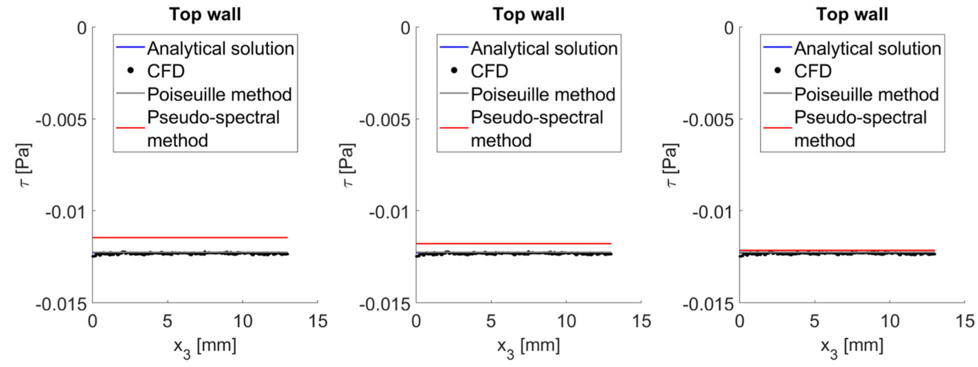

(a) (b) (c)

Fig. 7 Poiseuille flow WSS estimation when $R = 1.632 mm$, $\mu = 0.01 g/(cm \cdot s)$, and $u_{max} = 1 cm/s$. Three different approaches are compared against the analytical solution, WSS= -0.0123 *Pa*, i.e., CFD, Poiseuille method, and PSM. The latter is evaluated using an increasing number of harmonics: **a** $N = 5$, **b** $N = 10$, **c** $N = 40$

WSS can be estimated using Poiseuille-based methods and PSM, pretending that the velocity data are measured. Similar results are obtained when we use the analytical solution in place of CFD results directly to generate the data, showing that the numerical errors on the velocity field induced by the approximated geometry are very small in this case. Regardless of the source of the velocity data, either CFD results, or analytical solution, an additional source of error is introduced if the sample-velocity grid points do not coincide with the wall position. Hence, for the sake of comparison, in this idealized case, the grid spacing corresponds to the ultrasound resolution, but the position of the wall is explicitly enforced.

In particular, using the $H = 0.029$-mesh, results truncating the Fourier Series at 5, 10 and 40 harmonics (N) are shown in Table 2 and in a red solid line in Fig. 7a–c, respectively. The outputs are compared against the analytical solution (blue line), CFD computations (black markers), and the Poiseuille method (grey line). As expected, CFD and the Poiseuille method overlapped to the analytical solution and the PSM approaches the exact answer as the N increases. The errors in the average WSS estimation shown in Fig. 7a–c are 6.70e−2 ($N = 5$), 2.54e−2 ($N = 10$) and 1.06e−2 ($N = 40$), respectively. At $N = 40$ the error of the WSS is about two orders of magnitude larger than the result obtained from the CFD simulation (2.9e−4, see Table 1). This justifies using CFD as the ground truth in the absence of analytical solutions.

Remark The function approximated, in this case, is quadratic like the case considered in the Appendix with pseudo-spectral approximation. Here, however, the number of points used for the quadrature of the Fourier coefficients is limited by the resolution of the data. This causes some degradation of the accuracy for very high values of N (> 100), as the frequencies considered oscillate very rapidly with respect to the grid of available data.

Table 2 PSM: convergence (u_3 is the exact solution,$u_{3,N}$ its pseudo-spectral approximation, and N is the number of harmonics used in the truncated Fourier Series)

N	5	10	20	40
$\lVert u_3 - u_{3,N} \rVert_{L^2}$	0.0016	3.50E-04	4.51E-05	7.27E-06
$\left\lVert \frac{\partial u_3}{\partial x_3} - \frac{\partial u_{3,N}}{\partial x_3} \right\rVert_{L^2}$	0.0344	0.0162	0.0058	0.0021

Stenotic Channel

The previous case clearly represents an academic test, as, in general, coronaries are not perfectly cylindrical, particularly in the presence of plaques. In this second test, we consider the stenotic geometry described in "US Experimental Setup" Sect., Fig. 1.

To investigate in detail the role of (1) the geometry in the WSS estimation, and (2) the role of measurement errors, we present two tests, one based on the CFD results, and the other based on US Doppler measures.

A direct comparison of velocity data retrieved from CFD and from measures pinpoints the presence of discrepancies as the numerical velocity reaches 10 cm/s while the measures yield a maximum velocity of 8 cm/s. For this reason, we separate the analysis of the results in the two cases.

For the sake of a qualitative assessment, we notice however that in any case: (1) the maximum WSS occurs at the narrowest section of the vessel, (2) the stenotic wall presents higher WSS than the straight wall, (3) after the stenotic section, there is a sudden drop in the WSS on the top (stenotic) wall and a more gradual decrease on the bottom (non-stenotic) wall.

More quantitatively, the WSS peak values are in the order of 0.35 and 0.65 Pa for the bottom and top walls, respectively

WSS Estimation Based on CFD Velocity

We solved the Navier–Stokes equations in the stenotic geometry with our CFD solver, using the boundary conditions

Table 3 Mesh-independence test

Number of elements (x1000)	$\iint_S WSS\, dS$	Relative error	Domain of integration
1000	0.799792		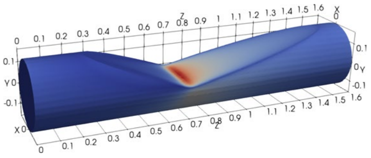
500	0.799794	2.50065E-06	
320	0.799799	8.75228E-06	
65	0.799793	1.25033E-06	
13	0.799801	1.12529E-05	
1000	0.698901		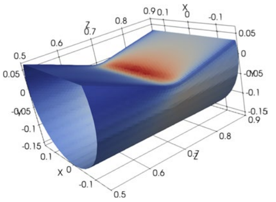
500	0.698902	1.10868E-06	
320	0.698902	8.52833E-07	
65	0.698896	8.27248E-06	
13	0.698890	1.62891E-05	
Number of elements (x1000)	**$\|\iint_V \boldsymbol{u}\, dV\|$**	**Relative error**	**Domain of integration**
1000	0.398938		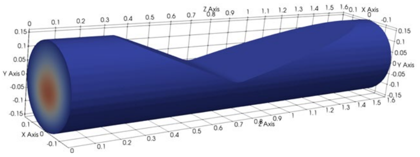
500	0.398571	9.20E-04	
320	0.397665	3.19E-03	
65	0.393270	1.42E-02	
13	0.378110	5.22E-02	

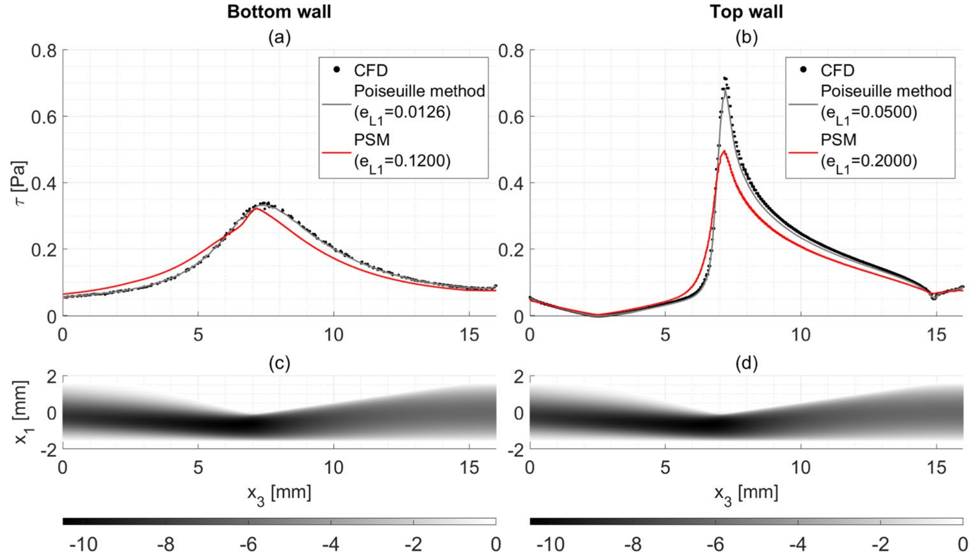

Fig. 8 WSS obtained by the Poiseuille and the PSM (N=5) using CFD data and benchmarked to CFD results: **a** Bottom (non-stenotic) wall, **b** Top (stenotic) wall, **c**–**d** velocity in the z-direction (the main stream runs from right to left). The average error e_{L1} is computed by summing the absolute differences between the estimated wall shear stress (WSS) values obtained from either the Poiseuille method or PSM and the WSS values obtained from computational fluid dynamics (CFD), divided by the total number of available data points

that reproduce the measurement settings. More details are reported in [42]. Precisely, the velocity profiles at the inflow along two orthogonal diameters were used to perform a bivariate spline interpolation providing velocity data at the inlet section. Null velocity conditions were prescribed at the walls, while traction-free open boundary conditions were prescribed at the outflow, i.e., $p\mathbf{n} - \mu\left(\nabla \boldsymbol{u} + \nabla^T \boldsymbol{u}\right) \cdot \mathbf{n} = \mathbf{0}$. The CFD quantities presented in this manuscript correspond to simulations obtained using a one-million-element mesh. The convergence tests are summarized in Table 3, wherein the integral of the Wall Shear Stress (WSS) is computed over both the entire geometry and the critical stenotic section. The results show that, even if we used the 1 M-element mesh, we would have obtained the same conclusion with a mesh with 0.5M elements.

The velocity obtained in this way was used to generate velocity data in the same plane used for US measures and with the same resolution. The data were eventually used to estimate the WSS. The latter was compared with the WSS computed by the CFD solver.

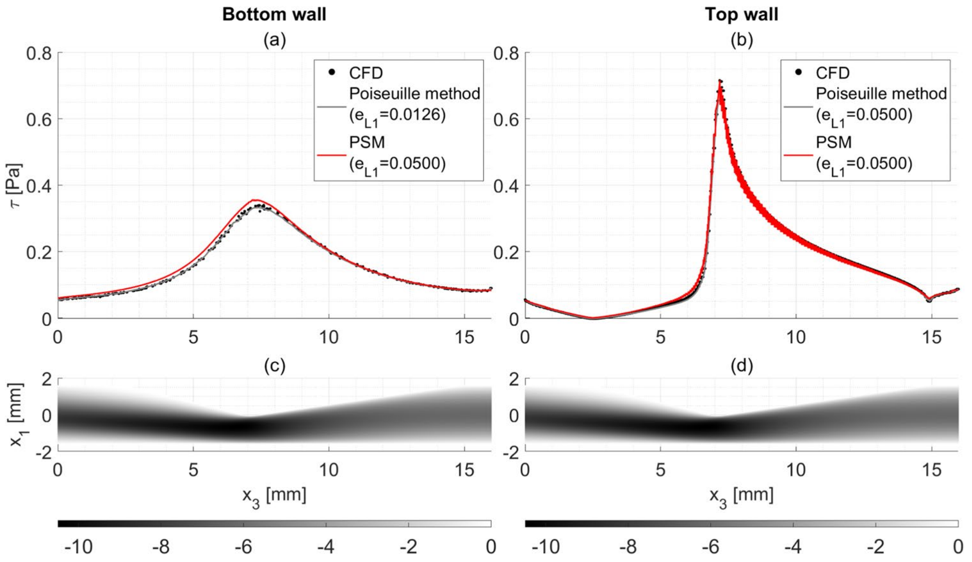

Fig. 9 WSS obtained by the Poiseuille and the PSM (N=15) using CFD data and benchmarked to CFD results: **a** Bottom wall, **b** Top wall, **c**–**d** velocity in the z-direction (the main stream runs from right to left) The average error e_{L1} is computed by summing the absolute differences between the estimated wall shear stress (WSS) values obtained from either the Poiseuille method or PSM and the WSS values obtained from computational fluid dynamics (CFD), divided by the total number of available data points

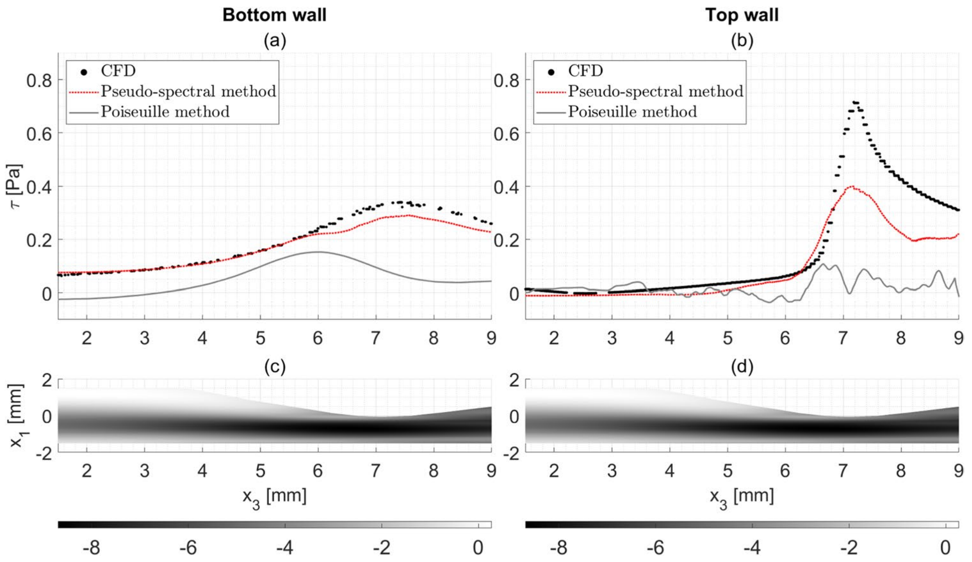

Fig. 10 WSS obtained by the Poiseuille and the PSM (N = 5) using ultrasound data and benchmarked to CFD results: **a** Bottom wall, **b** Top wall, **c**–**d** velocity in the z-direction (the main stream runs from right to left)

Figures 8 and 9 show WSS values obtained from the PSM using 5 and 15 harmonics, respectively. Each figure includes 4 plots: (a–b) WSS obtained from CFD (black markers), from velocity using the Poiseuille (grey line) and the PSM (red line); (c–d) top view of the CFD velocity z-component, which helps to understand qualitatively the WSS computations; the stenosis is located at 7 mm. The figures present the result along the top and the bottom wall of the geometry displayed in the panels (c–d).

The figures show, on one hand, that the Poiseuille method accurately predicts the WSS when CFD velocity is used as input. In this case, the neglected terms (axial velocity, wall shape, and velocity variation in the axial direction) do not play a significant role. On the other hand, as expected, the PSM underestimates the WSS computation when $N = 5$. The difference vanishes as the number of harmonics increases (Fig. 9). The results of the two numerical techniques at this point are the same.

WSS estimation based on US measures

Figures 10, 11, 12, and 13 present the results of the real case when the velocity is obtained from US measures. These figures differ in the number of harmonic selected for the PSM, $N = 5, 8, 10,$ and 12, respectively. The impact of measurement errors is apparent, particularly for the

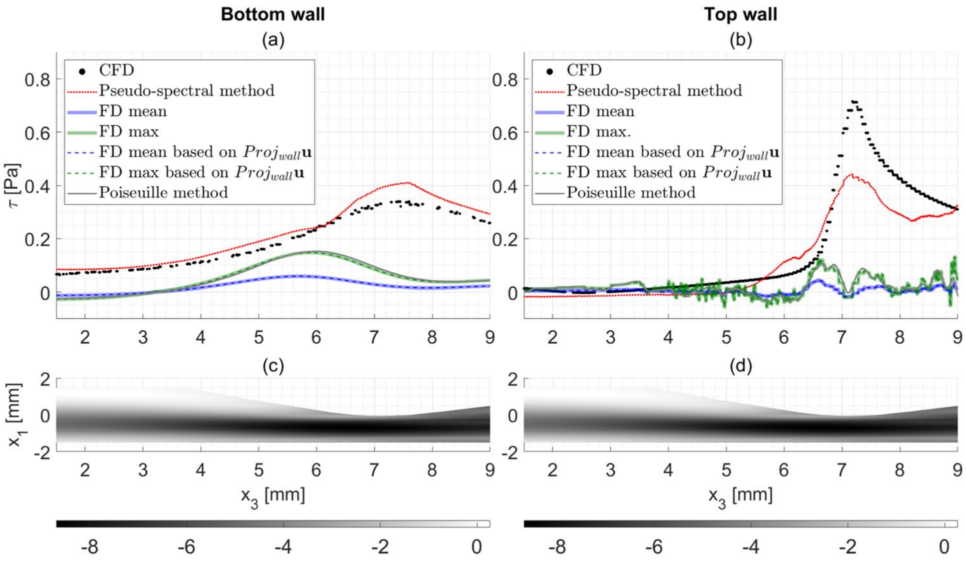

Fig. 11 WSS obtained by the Poiseuille and the PSM (N = 8) using ultrasound data and benchmarked to CFD results: **a** Bottom wall, **b** Top wall, **c**–**d** velocity in the z-direction (the main stream runs from right to left). FD stands for Finite Difference and refers to the methods in Ref. [35], using both the strategy of averaging different measures or tagging the maximum velocity

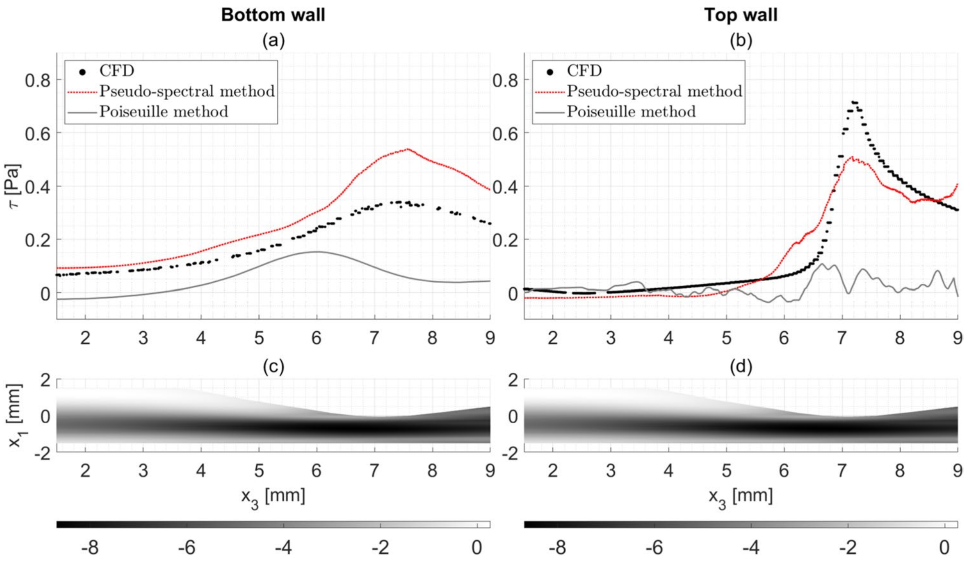

Fig. 12 WSS obtained by the Poiseuille and the PSM (N=10) using ultrasound data and benchmarked to CFD results: **a** Bottom wall, **b** Top wall, **c**–**d** velocity in the z-direction (the main stream runs from right to left)

Poiseuille-based methods. On the straight wall (bottom), the peak WSS estimated by the Poiseuille is under-predicted (0.15 Pa) (dissipation error), and the position is shifted downstream with respect to the narrowest section (dispersion error). On the stenotic wall, the WSS estimation does not provide any clear trend, and values oscillate erratically with poor connection to the geometry of the studied case.

In the PSM, when five harmonics are used (Figs. 10a–b), the outcome is consistent in general with results based on CFD velocity data (Figs. 8a–b), and the qualitative phenomenology is met. More specifically: (1) the maximum WSS is aligned to the narrowest section of the vessel; (2) the stenotic wall presents higher WSS than the straight wall; (3) after the stenotic section, there is a sudden drop in the WSS on the top wall and a more gradual decrease on the bottom wall.

The WSS peak values are in the order of 0.25 and 0.35 Pa for the straight and stenotic walls, respectively, which undershoots CFD estimations (0.35 and 0.65, respectively). Nonetheless, undershooting was anticipated for two reasons. First, the velocity magnitudes are smaller in the ultrasound data than in the CFD simulation. Second, the truncation of a Fourier series is expected to introduce dissipation errors, as already happened when five harmonics were used in the CFD case, when the maximum WSS were 0.30 and 0.45 Pa, respectively.

Unlike the case when CFD velocity data is input, increasing the number of harmonics makes minor improvements in terms of accuracy (Figs. 12 and 13a, b). The lack of regularity in the data and the noise prevent the convergence.

Visual inspection of the velocity profiles obtained with the DFT helps identify a good value of N for the truncation.

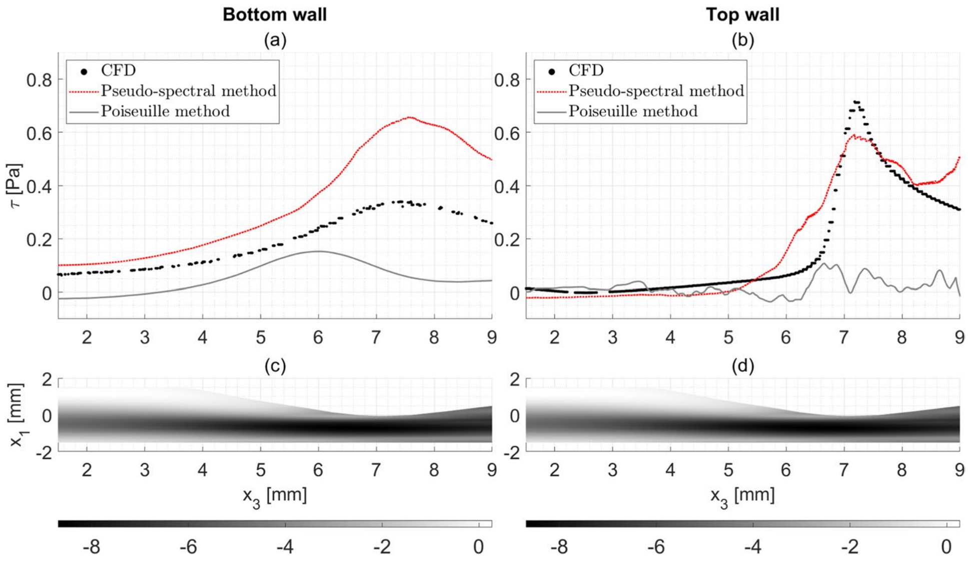

Fig. 13 WSS obtained by the Poiseuille and the PSM (N=12) using ultrasound data and benchmarked to CFD results: **a** Bottom wall, **b** Top wall, **c**–**d** velocity in the z-direction (the main stream runs from right to left)

Table 4 Evaluation of method accuracy using L^1-norm Error (e_{L1})

N	Bottom wall		Top wall	
	Poiseuille method	PSM	Poiseuille method	PSM
5	1.3377	0.1090	1.0861	0.3866
8		0.1409		0.3002
10		0.4458		0.2657
12		0.7740		0.3156
15		1.3790		0.6754

Table 5 Evaluation of method accuracy using L^2-norm error (e_{L2})

N	Bottom wall		Top wall	
	Poiseuille method	PSM	Poiseuille method	PSM
5	0.0221	0.0022	0.0139	0.0051
8		0.0026		0.0039
10		0.0079		0.0033
12		0.0136		0.0042
15		0.0241		0.0082

If unrealistic oscillations appear, fewer harmonics should be recommended. Selecting the proper number of harmonics is a trade-off between underestimating the WSS and introducing artificial oscillations at data discontinuities.

For the particular case under study, the comparison with CFD results reveals that adopting $N = 8$ minimized the differences between the WSS benchmark values and those obtained by the PSM. Tables 4 and 5 illustrate this comparison using two metrics, respectively: (1) the average error e_{L1}[2], and (2) the L2-Norm Error e_{L2}.[3] When $N = 8$, the average error obtained by the Poiseuille-based methods is 9 times larger than the PSM error on the bottom wall, and 3 times larger on the top wall. PSM features an error of 0.14Pa on average from the CFD benchmark on the bottom wall, and 0.30Pa on the top wall. The discrepancies are accentuated after the narrowest section of the vessel. As we discuss more in detail in the next Section, this discrepancy may potentially stem from the experimental setup. The transducer, positioned on the left side, measures flow from right to left, resulting in signal decay as distance increases from the transducer. The interference from the top wall may exacerbate this decay, particularly noticeable after the narrowest section, possibly leading to velocity underestimation and consequently underestimated WSS. This hypothesis requires further investigation and verification.

For the sake of comparison, Figure 11 includes two additional methods for evaluating WSS using Finite Differences (FD) to estimate the shear rate ($\partial u_3/\partial r$). In one approach (green), the maximum shear rate, evaluated in the neighborhood of each wall, is multiplied by the kinematic viscosity μ [62]. In the other approach (blue), an average of the neighborhood shear rate is utilized. Specifically, in this case, the average is calculated from the 6 data points closest to each

---

[2] The average error e_{L1} is computed by summing the absolute differences between the estimated Wall Shear Stress (WSS) values obtained from either the Poiseuille-based methods or PSM and the WSS values obtained from computational fluid dynamics (CFD), divided by the total number of available data points.

[3] The L2-Norm Error e_{L2} is computed by taking the square root of the sum of squared differences between the estimated WSS values obtained from either the Poiseuille method or PSM and the WSS values obtained from CFD, divided by the total number of available data points.

Footnote 3 (continued)

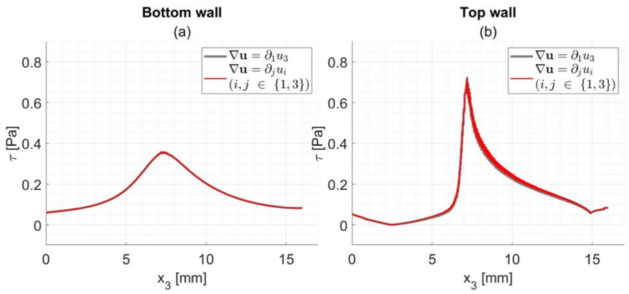

Fig. 14 Effect of dropping the lateral velocity component and axial derivatives on WSS computation using the pseudo spectral method truncated at 15 harmonics based on CFD-data: **a** Bottom wall, **b** Top wall

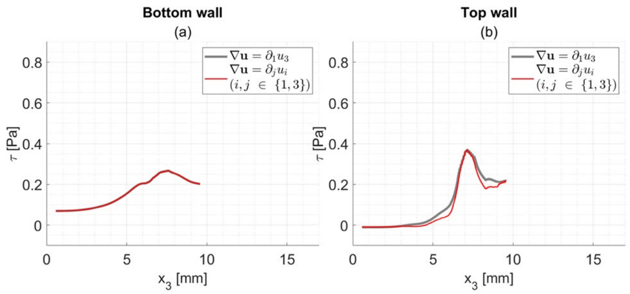

Fig. 15 Effect of dropping the lateral velocity component and axial derivatives on WSS computation using the pseudo spectral method truncated at five harmonics based on ultrasound-data: **a** Bottom wall, **b** Top wall

wall [35]. Similar results are obtained when the computations employ the projected velocity onto the wall instead of the axial velocity u_3 (dashed lines of the same corresponding colors). In this particular case, the choice between using the axial velocity u_3 or the projected velocity onto the wall doesn't seem to yield a noticeable difference in results. This lack of distinction likely arises due to the experimental setup, where the observation line passes through the axis of the vessel. Additionally, it's notable that results obtained using the maximum shear rate method are comparable to those obtained by the Poiseuille method, as both methods differ only in their approach to evaluate the partial derivative $\frac{\partial u_3}{\partial r}$. The Poiseuille method appears smoother because an average kernel was applied before plotting the results. However, when using average values, a smoothing effect occurs, which filters noise but also introduces error, resulting in reduced estimations for the WSS.

Effect of Dropping the Lateral Component of Velocity

As the vessel geometry deviates from a perfect cylinder, lateral components of velocity and variation of the velocity in the axial direction appear. Although the axial velocity and its variation in the lateral direction dominate the flow, in principle, the remaining components should not be dropped. In this Section, we present the effect of dropping those secondary components in practice.

Figure 14 compares the effect of including (red line) or dropping (gray line) the $\partial u_1/\partial x_1$, $\partial u_1/\partial x_3$, $\partial u_3/\partial x_3$ in the PSM when CFD data is used as input and $N = 15$. Results are almost identical; hence, for this particular case, one can conclude that $\partial u_3/\partial x_1$ dominates the computation of the WSS, and the remaining terms can be neglected, as done by the Poiseuille method.

Analogously, Fig. 15 presents the same comparison when ultrasound data is input and $N = 5$. In this case, some deviation is observed in the stenotic wall (top wall), precisely at the locations where the normal vector deviates from the unit vector $\mathbf{e}_1$. Nonetheless, main trends, maximum and minimum values are not significantly affected. We conclude that, in our test, setting WSS$\approx \mu \partial u_3/\partial x_1$ is a reliable approximation. We discuss this point further later on.

Discussion

Analytical and Noise-Free Data

When the data are retrieved from either the analytical solution or accurate CFD simulations, the Poiseuille-based approach, based on polynomial interpolation, works properly. Results are accurate from both the mathematical and the clinical points of view.

In the cases considered here, dropping the axial derivatives of the radial and axial components and the axial derivative of the radial component did not significantly affect the results. This was obviously expected in the Poiseuille flow text case, where the dropped components are null. In the stenotic case, this result is not trivial, yet quite evident.

With accurate data, the pseudo-spectral approach with an appropriate number of harmonics matches the accuracy of the polynomial interpolation.

The results obtained by including the axial component and derivatives do not deviate significantly from the cases when these components are dropped. However, it is worth emphasizing that these conclusions correspond only to one particular case when the axis of the (stenotic) pipe was rectilinear. Hence, they should not be generalized, and a systematic study over a wide range of stenotic geometries is needed for that purpose.

Real Data

When we apply the different methods to a real data set, the performances are very different. Poiseuille-based methods

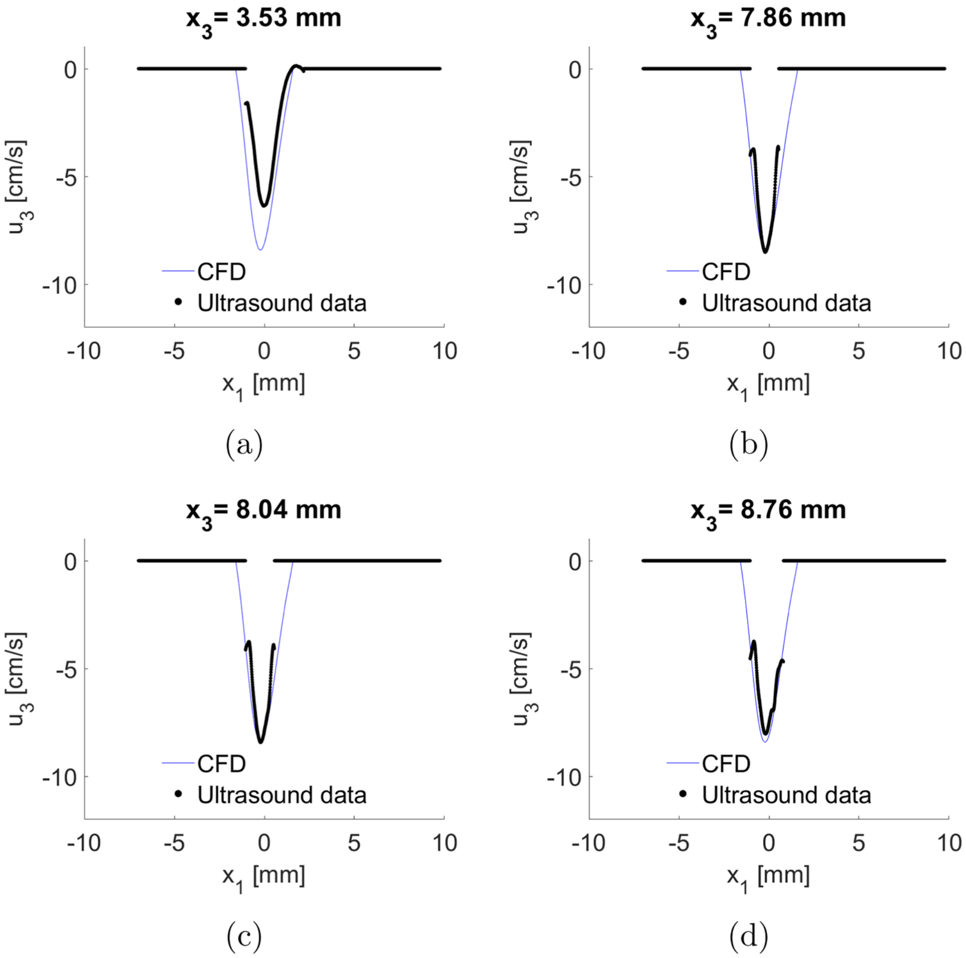

Fig. 16 CFD velocity profiles (blue) vs. US Data for different values of the axial coordinate: **a** $x_3 = 3.53\,mm$; **b** $x_3 = 7.86\,mm$; **c** $x_3 = 8.04\,mm$; **d** $x_3 = 8.76\,mm$.

suffer from the noise in the measures, to the point that the WSS estimation looses reliability. This is particularly true for the stenotic wall (top wall presented in Figs. 10, 11, 12, and 13). Also the methods proposed in [35], being based on the Poiseuille assumption and a FD approximation of the derivatives (see Appendix), suffer from noise in the data, even if the average of the evaluations potentially mitigate this aspect.

On the contrary, the PSM provides results that reproduce the pattern of the CFD results. The impact of the noise in the estimation is apparent when we include more terms in the truncated Fourier series. The selection of the value N of the truncation should realize a trade-off between the accuracy and the denoising. In particular, the comparison of the results for $N = 5, 8, 10, 12, 15$ shows that

1. the values $N = 5$ and 8 give good results on the straight wall and an underestimation of the WSS on the stenotic wall;
2. increasing the terms in the series improves the estimation on the stenotic side but degrades it on the straight wall.

The WSS is lower on the straight side, so for a uniformly distributed noise, we argue that the Signal-to-Noise Ratio (SNR) is lower on this side. Correspondingly, the noise shows up for a lower number of harmonics than for the stenotic side of the vessel.

This suggests that the choice of N may be related to the position on the wall in correspondence with an estimation of the SNR. We may notice, however, that the pattern of the WSS is correctly captured on the stenotic side also for $N = 8$, with a good localization of the WSS peak. We conclude that $N = 8$ is a good choice for both sides, if we focus only on the stenotic side $N = 12$ performs the best.

To understand better the discrepancies between the WSS estimations and the CFD results, one needs to consider the nature of the input data. Close-to-the-wall, data may be inaccurate, and small measurement errors can drastically affect the derivative estimation, particularly the one based on the polynomial interpolation. Due to the segmentation in which the pixels containing the wall were set to zero, ultrasound-measured velocity values near the wall may not approach zero smoothly, as one would expect, further contributing to inaccuracies in the estimation of WSS. Along the same line, the PSM displays a systematic overestimation of the WSS around 8 mm on the stenotic wall.

In Fig. 16, we report the CFD velocity profiles compared with the US data. Here the stenotic side is on the right. The discrepancy between the wall localization in the CFD and the data on the stenotic side is apparent, as well as a sudden variation of velocity in the axial direction in some data around the boundary. For low values of x_3 (Fig. 16a), the difference is much smaller, than for x_3 around 8 mm. We argue that this is the reason for the accuracy degradation in this region. However, overall the pseudo-spectral approach reveals to be a robust tool, able to filter the noise of the US data and obtain a clinically accurate estimation of the WSS.

Use of Real Geometries

The technique proposed here can be promptly extended to the case of 3D, extending the computation of the shear-rate tensor to the out-of-plane components with the same approach used for the axial velocity. However, currently we have only 2D data and this potentially undermines the accuracy in real 3D geometries, in the presence of significant out-of-plane velocity components. It is worth stressing that this is a limitation of the available data, not of the methodology *per se*. In the follow-up, we will consider 3D US data for the WSS estimation using the PSM.

Conclusions and Perspectives

In this paper, a new approach for quantifying wall shear stress (WSS) in coronary arteries using Doppler US imaging is presented. WSS is a critical parameter for predicting potential adverse events in cardiovascular and coronary diseases. A reliable tool based on US data for the estimation of the WSS is, therefore, an important contribution to avoiding patient-specific CFD.

Our method aims to improve the accuracy of WSS estimation by considering two factors. First, it takes into account the directional variation of the two available velocity components and vessel wall shape. Secondly, it copes with the presence of measurement errors by using the Discrete Fourier Transform (DFT) to interpolate the velocity data. The conceptual novelty of our proposal relies mainly on using a Fourier-based differentiation as opposed to classical polynomial interpolation techniques that lead to classical FD schemes (see Appendix). The advantage of the pseudo-spectral method is that it relies on a harmonic analysis of the data, so it naturally differentiates low and high-frequencies. Since the noise in the data can be regarded as a high-frequency perturbation, truncating the Fourier series introduces naturally a de-noising filtering. To the best of our knowledge, this approach was never used in the existing literature.

The approach was tested in two cases: a pipe with straight walls (Poisseuille flow) and a stenotic case. The results were compared against analytical solutions, Computational Fluid Dynamics (CFD) results, and the Poiseuille method, a methodology used in the literature that depends only on the radial velocity of the closest three to four pixels to the vessel wall. CFD-based WSS results were used as a benchmark. Poiseuille-based methods are accurate under idealized conditions but lack reliability when using ultrasound imaging data. In contrast, the PSM is reliable also when using real data, with proper calibration of the Fourier approximation. In principle, the new method converges to the actual solution as the number of harmonics increases. However, when using ultrasound imaging data, increasing the number of harmonics introduces noise into the estimation, reducing the overall accuracy.

With appropriate calibration of the Fourier series truncation, the WSS pattern was reconstructed with very good accuracy for what concerns the relevant information from the clinical point of view. Nevertheless, PSM has clearly its own limitations. It is not exact, since the computation of the Fourier coefficients necessarily relies on numerical quadrature. Also, the computations of the derivatives of the axial velocity suffers from the approximations induced by the data collection in the domain and not exactly on the boundary of the coronary.

Upcoming research will involve extensive testing on more complex and even patient-specific geometries [42], to assess precisely the role of the axial component and derivatives in the final WSS estimation. Should 3D data - including out-of-plane components - be available, we will extend the approximation to the inclusion of the circumferential components of the velocity. Another important topic will be the automatic selection of the number N of harmonics to include, possibly as a space-dependent function of the SNR. One possible approach is to use artificial neural networks that have been trained on CFD results from different stenotic geometries, which could provide the user with an educated selection of the parameter N.

Appendix A Recap of Approximation and Differentiation Errors

In this Section, we recall some basic concepts of numerical analysis for the interpolation of functions and for the corresponding differentiation.

Polynomial Interpolation

Let us recall some basic results of polynomial interpolation (see e.g. [58]). Let us denote by $L^2([a,b])$ the space of functions *f* such that $\int_a^b f^2(x)dx < \infty$ (in the Lebesgue sense). The corresponding norm reads $\|f\|_{L^2} \equiv \left(\int_a^b f^2(x)dx\right)^{1/2}$.

Let us denote by $\Pi_f^k(x)$ the interpolating polynomial of the values of *f* on equispaced nodes with step *h* and degree *k*. We assume that *f* is an L^2 function together with its first *s* (distributional) derivatives. Then, we can prove that

$$\|f - \Pi_f^k\|_{L^2} \leq Ch^{k+1}\|f^{(s)}\|_{L^2}, \quad \|f' - p_k'\|_{L^2} \leq Ch^k\|f^{(s)}\|_{L^2}.$$

Here, $f^{(s)}$ denotes the derivative of order *s* of *f*. Also, here and in the sequel *C* will denote a constant (not necessarily the same in each occurrence) independent of the discretization parameters (*h* and *k*). In the case of the Poiseuille formula, the interpolation currently adopted refers to either a degree $k = 2$ on three nodes or $k = 3$ on four nodes (including the point on the wall where the velocity is 0).

Notice that if the values of *f* used for the interpolation are affected by noise, i.e. the interpolation relies on values $\widetilde{f}_i = f_i + v_i$ where v_i is a measurement error, it is possible to prove that

$$\max_x |\Pi_f^k - \Pi_{\tilde{f}}^k| \leq \Lambda_k \max_i |v_i|$$

where Λ_k (known as Lebesgue constant) scales with *k* like $2^{k+1}/(ek\log(k))$ (*e* is the Neper number).

Combining these results, we have that the approximation error in the presence of noise reads

$$\begin{aligned}\|f - \Pi_{\tilde{f}}^k\|_{L^2} \leq& \|f - \Pi_f^k\|_{L^2} + \|\Pi_f^k - \Pi_{\tilde{f}}^k\|_{L^2} \\ \leq& Ch^{k+1}\|f^{(s)}\| + \Lambda_k\sqrt{I}\max_i |v_i|,\end{aligned}$$

where *I* is the length of the interpolation interval.

We are specifically interested in assessing the impact of the noise on the derivative. Notice that the interpolating polynomial can be written in the Lagrange form:

$$\Pi_f^k = \sum_j f_j\varphi_j, \quad \Pi_{\tilde{f}}^k = \sum_j \widetilde{f}_j\varphi_j$$

where *j* ranges on the interpolation nodes and

$$\varphi_j(x) = \frac{\prod_{l,l\neq j}(x - x_l)}{\prod_{l,l\neq j}(x_j - x_l)}.$$

We have therefore

$$\left(\Pi_f^k - \Pi_{\tilde{f}}^k\right)' = \sum_j v_j\varphi_j'.$$

Specifically,

$$\varphi_j' = \frac{1}{\prod_{l,l\neq j}(x_j - x_l)} \sum_m \prod_{l,l\neq j,l\neq m} (x - x_l). \tag{11}$$

Notice that the terms of the sum in Eq. (11), when evaluated in the interpolating nodes (as we do for our estimation of the WSS) do not vanish altogether simultaneously and scale like h^{k-1}, while the denominator scales like h^k, so that

$$|\left(\Pi_f^k - \Pi_{\tilde{f}}^k\right)'| \leq C\frac{\max_j |v_j|}{h}.$$

Setting $|v_{max}| \equiv \max_j |v_j|$, we conclude

$$\|\left(f - \Pi_{\tilde{f}}^k\right)'\| \leq Ch^k\|f^{(s)}\| + C\frac{|v_{max}|}{h}. \tag{12}$$

This inequality pinpoints the potential lack of robustness of the derivative in the presence of noise, as *h* is related to the resolution of the measurements (in our case, order of microns), so it is generally quite small. In the presence of purely random noise (no systematic errors), v_j will be uncorrelated to $v_{j\pm1}$, so the previous estimate cannot be improved. The result is that the term $\frac{|v_{max}|}{h}$ can significantly pollute the quality of the approximation.

Pseudospectral DFT derivative

When we use the pseudospectral derivative, from the mathematical point of view we replace the derivative of the function with the derivative of its (generalized) discrete Fourier series. This means that we write the original function with the Fourier series

$$f = \sum_{j=1}^{\infty} c_j\psi_j$$

where ψ_j, in our case, is the set of sinusoidal functions with increasing frequency and

$$c_j = \frac{\int_a^b f\psi_j dx}{\int_a^b \psi_j^2 dx} \tag{13}$$

with the integrals computed over the approximation interval. If we replace *f* with the truncation $f_N = \sum_{j=1}^{N} c_j\psi_j$, the error reads $\sum_{j=N+1}^{\infty} c_j\psi_j$. Since from the Fourier theory $c_j \to 0$ for $j \to \infty$, the coefficient c_{N+1} provides the leading term of the approximation error.

In our approach, *f* is approximated by the truncated series

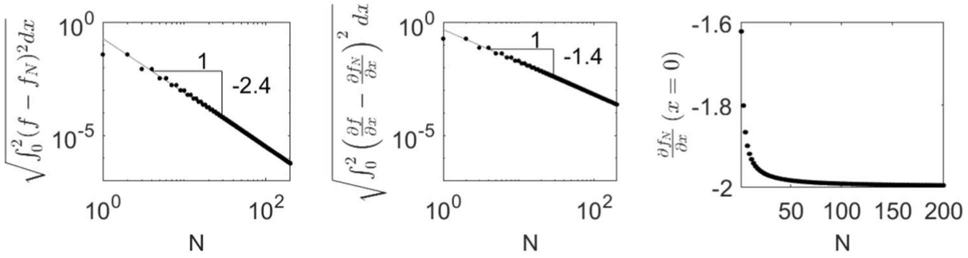

(a) (b) (c)

Fig. 17 Difference between the quadratic function $f(x) = x(x - 2)$ and its corresponding truncated sine Fourier series $\hat{f}_N(x) = \sum_{k=1}^{N} \hat{c}_k \sin(\frac{k\pi}{2}x)$ as the number of terms N increases in the Fourier series (evaluated in the interval [0, 2]): **a** distance between functions, **b** distance between function derivatives, **c** Derivative value of the truncated Fourier series at $x = 0$.

$$\Pi_f^N = \sum_{j=1}^{N} \hat{c}_j \psi_j$$

where the $\hat{c}_j$ are obtained by numerical quadrature of the (13) involving the available measures. Specifically, we resort here to the well-known Discrete Fourier Transform (DFT) [58, 63].

The theoretical estimates available for the DTF derivative state that the error decays like $N^{-(r+1)}$ if a function is differentiable r times in the interval of interest (including the end-points), and its first derivative error decays like N^{-r}. The convergence rate strictly depends on the regularity of the function.

To exemplify these theoretical results, the quadratic function $f(x) = x^2 - 2x$ in [0, 2] is selected to test the pseudo-spectral derivative. Here, f is regarded as the portion in [0, 2] of a periodic odd function.

Figure 17a shows in a logarithmic scale how $d(f, f_N) = \left(\int_0^2 (f - f_N)^2 dx\right)^{1/2}$ converges to zero as N increases. This quantifies the error of the truncation. Similarly, Fig. 17b shows the convergence of the difference between their corresponding derivatives. The slopes of the error in logarithmic scales confirm that the derivative errors converge one order less than the values. The specific orders (≈ 2.4 and ≈ 1.4) depend on the regularity of the periodic replica of our function.

Figure 17c shows $\frac{d\hat{f}_N}{dx}$ at $x = 2$ (where the coefficients are computed with a trapezoidal quadrature formula), which eventually converges to $\frac{df}{dx}(x = 2) = -2.0$. For example, the derivative error is close to 20% for $N = 1$ and 5% for $N = 5$.

A significant advantage of the pseudo-spectral derivative in this field is the robustness in the presence of noise. Specifically, we argue that, in the absence of systematic errors (to be eliminated by accurate measurements devices and tuning), the noise is a function $v(x)$ with components in high frequency, i.e.

$$\widetilde{f} = f + v = \sum_{j=1}^{\infty} (c_j + d_j)\psi_j$$

where the Fourier coefficients d_j of the noise function v are small for j small and high for large js. With this assumption, we have, for an r-differentiable function,

$$\begin{aligned} \|\left(f - \Pi_{\widetilde{f}}^N\right)'\|_{L^2} &\leq \|\left(f - \Pi_f^N\right)'\|_{L^2} + \|\left(\Pi_f^N - \Pi_{\widetilde{f}}^N\right)'\|_{L^2} \\ &\leq \mathcal{O}(N^{-r}) + \|\sum_{j=1}^{N} d_j \psi_j'\|_{L^2}. \end{aligned}$$

Let us assume that the noise is negligible for $j < M$, i.e., $d_j \approx 0$ for $j \leq M$. If we select $N < M$, we conclude that our pseudo-spectral approximation is not affected by the noise. More in general, from the practical point of view, the selection of N needs to realize the trade-off between the accuracy (first term at the right-hand side of the last inequality) and the robustness to the noise (second term). This is exactly what we did in our WSS estimation from real measures.

Acknowledgements The support of the National Institutes of Health (NIH) R01EB031101 is gratefully acknowledged. A.V. would like to acknowledge also research funding support by the National Science Foundation (NSF) under Award Number DMS2012286 (PI: A. Veneziani, with O. San and T. Iliescu) and DMS2038118 (PI: J. Nagy).

Declarations

Conflict of interest The authors have no financial or proprietary interests in any material discussed in this article.

References

1. Dhawan, S. S., R. P. Avati Nanjundappa, J. R. Branch, W. R. Taylor, A. A. Quyyumi, H. Jo, M. C. McDaniel, J. Suo, D. Giddens, and H. Samady. Shear stress and plaque development. *Expert Review of Cardiovascular Therapy*. 8(4):545–556, 2010.
2. Makris, G., A. Nicolaides, X. Xu, and G. Geroulakos. Introduction to the biomechanics of carotid plaque pathogenesis and rupture:

review of the clinical evidence. *The British Journal of Radiology*. 83(993):729–735, 2010.

3. Corban, M. T., P. Eshtehardi, J. Suo, M. C. McDaniel, L. H. Timmins, E. Rassoul-Arzrumly, C. Maynard, G. Mekonnen, S. King 3rd., A. A. Quyyumi, et al. Combination of plaque burden, wall shear stress, and plaque phenotype has incremental value for prediction of coronary atherosclerotic plaque progression and vulnerability. *Atherosclerosis*. 232(2):271–276, 2014.
4. Slager, C., J. Wentzel, F. Gijsen, J. Schuurbiers, A. Wal, A. Van Der Steen, and P. Serruys. The role of shear stress in the generation of rupture-prone vulnerable plaques. *Nature Clinical Practice Cardiovascular Medicine*. 2(8):401–407, 2005.
5. Samady, H., P. Eshtehardi, M. C. McDaniel, J. Suo, S. S. Dhawan, C. Maynard, L. H. Timmins, A. A. Quyyumi, and D. P. Giddens. Coronary artery wall shear stress is associated with progression and transformation of atherosclerotic plaque and arterial remodeling in patients with coronary artery disease. *Circulation*. 124(7):779–788, 2011.
6. Eshtehardi, P., A. J. Brown, A. Bhargava, C. Costopoulos, O. Y. Hung, M. T. Corban, H. Hosseini, B. D. Gogas, D. P. Giddens, and H. Samady. High wall shear stress and high-risk plaque: an emerging concept. *The International Journal of Cardiovascular Imaging*. 33(7):1089–1099, 2017.
7. Stone, P. H., S. Saito, S. Takahashi, Y. Makita, S. Nakamura, T. Kawasaki, A. Takahashi, T. Katsuki, S. Nakamura, A. Namiki, et al. Prediction of progression of coronary artery disease and clinical outcomes using vascular profiling of endothelial shear stress and arterial plaque characteristics: the prediction study. *Circulation*. 126(2):172–181, 2012.
8. Kumar, A., O. Y. Hung, M. Piccinelli, P. Eshtehardi, M. T. Corban, D. Sternheim, B. Yang, A. Lefieux, D. S. Molony, E. W. Thompson, et al. Low coronary wall shear stress is associated with severe endothelial dysfunction in patients with nonobstructive coronary artery disease. *JACC: Cardiovascular Interventions*. 11(20):2072–2080, 2018.
9. Kumar, A., E. W. Thompson, A. Lefieux, D. S. Molony, E. L. Davis, N. Chand, S. Fournier, H. S. Lee, J. Suh, K. Sato, et al. High coronary shear stress in patients with coronary artery disease predicts myocardial infarction. *Journal of the American College of Cardiology*. 72(16):1926–1935, 2018.
10. Gijsen, F., Y. Katagiri, P. Barlis, C. Bourantas, C. Collet, U. Coskun, J. Daemen, J. Dijkstra, E. Edelman, P. Evans, et al. Expert recommendations on the assessment of wall shear stress in human coronary arteries: existing methodologies, technical considerations, and clinical applications. *European Heart Journal*. 40(41):3421–3433, 2019.
11. Perinajová, R., J. F. Juffermans, J. J. Westenberg, R. L. Palen, P. J. Boogaard, H. J. Lamb, and S. Kenjereš. Geometrically induced wall shear stress variability in CFD-MRI coupled simulations of blood flow in the thoracic aortas. *Computers in Biology and Medicine*. 133:104385, 2021.
12. Karmonik, C., C. Yen, O. Diaz, R. Klucznik, R. G. Grossman, and G. Benndorf. Temporal variations of wall shear stress parameters in intracranial aneurysms-importance of patient-specific inflow waveforms for CFD calculations. *Acta Neurochirurgica*. 152(8):1391–1398, 2010.
13. Oyre, S., S. Ringgaard, S. Kozerke, W. P. Paaske, M. B. Scheidegger, P. Boesiger, and E. M. Pedersen. Quantitation of circumferential subpixel vessel wall position and wall shear stress by multiple sectored three-dimensional paraboloid modeling of velocity encoded cine MR. *Magnetic Resonance in Medicine*. 40(5):645–655, 1998.
14. Oyre, S., W. P. Paaske, S. Ringgaard, S. Kozerke, M. Erlandsen, P. Boesiger, and E. Pedersen. Automatic accurate non-invasive quantitation of blood flow, cross-sectional vessel area, and wall shear stress by modelling of magnetic resonance velocity data. *European Journal of Vascular and Endovascular Surgery*. 16(6):517–524, 1998.
15. Stokholm, R., S. Oyre, S. Ringgaard, H. Flaagoy, W. Paaske, and E. Pedersen. Determination of wall shear rate in the human carotid artery by magnetic resonance techniques. *European Journal of Vascular and Endovascular Surgery*. 20(5):427–433, 2000.
16. Cheng, C. P., D. Parker, and C. A. Taylor. Quantification of wall shear stress in large blood vessels using Lagrangian interpolation functions with cine phase-contrast magnetic resonance imaging. *Annals of Biomedical Engineering*. 30(8):1020–1032, 2002.
17. Stalder, A. F., M. Russe, A. Frydrychowicz, J. Bock, J. Hennig, and M. Markl. Quantitative 2d and 3d phase contrast MRI: optimized analysis of blood flow and vessel wall parameters. *Magnetic Resonance in Medicine: An Official Journal of the International Society for Magnetic Resonance in Medicine*. 60(5):1218–1231, 2008.
18. Markl, M., W. Wallis, and A. Harloff. Reproducibility of flow and wall shear stress analysis using flow-sensitive four-dimensional MRI. *Journal of Magnetic Resonance Imaging*. 33(4):988–994, 2011.
19. Szajer, J., and K. Ho-Shon. A comparison of 4d flow MRI-derived wall shear stress with computational fluid dynamics methods for intracranial aneurysms and carotid bifurcations—a review. *Magnetic Resonance Imaging*. 48:62–69, 2018.
20. Pantos, I., G. Patatoukas, E. P. Efstathopoulos, and D. Katritsis. In vivo wall shear stress measurements using phase-contrast MRI. *Expert Review of Cardiovascular Therapy*. 5(5):927–938, 2007.
21. Hong, J., M. Su, Y. Yu, Z. Zhang, R. Liu, Y. Huang, P. Mu, H. Zheng, and W. Qiu. A dual-mode imaging catheter for intravascular ultrasound application. *IEEE Transactions on Medical Imaging*. 38(3):657–663, 2018.
22. Janjic, J., F. Mastik, M. D. Leistikow, J. G. Bosch, G. Springeling, A. F. Steen, and G. Soest. Sparse ultrasound image reconstruction from a shape-sensing single-element forward-looking catheter. *IEEE Transactions on Biomedical Engineering*. 65(10):2210–2218, 2018.
23. Lindsey, B. D., B. Jing, S. Kim, G. C. Collins, and M. Padala. 3-d intravascular characterization of blood flow velocity fields with a forward-viewing 2-d array. *Ultrasound in Medicine & Biology*. 46(9):2560–2571, 2020.
24. Kim, S., B. Jing, Jimena Martin Tempestti, Alessandro Veneziani, and B. D. Lindsey. Wall shear stress estimation in coronary arteries using forward-viewing, high frequency ultrasound: a phantom study in comparison with computational fluid dynamics. *Ultrasonics*. 117:106558, 2021.
25. Gates, P. E., A. Gurung, L. Mazzaro, K. Aizawa, S. Elyas, W. D. Strain, A. C. Shore, and R. Shandas. Measurement of wall shear stress exerted by flowing blood in the human carotid artery: ultrasound doppler velocimetry and echo particle image velocimetry. *Ultrasound in Medicine & Biology*. 44(7):1392–1401, 2018.
26. Blake, J. R., S. Meagher, K. H. Fraser, W. J. Easson, and P. R. Hoskins. A method to estimate wall shear rate with a clinical ultrasound scanner. *Ultrasound in Medicine & Biology*. 34(5):760–774, 2008.
27. Mynard, J. P., B. A. Wasserman, and D. A. Steinman. Errors in the estimation of wall shear stress by maximum doppler velocity. *Atherosclerosis*. 227(2):259–266, 2013.
28. Mynard, J. P., and D. A. Steinman. Effect of velocity profile skewing on blood velocity and volume flow waveforms derived from maximum doppler spectral velocity. *Ultrasound in Medicine & Biology*. 39(5):870–881, 2013.
29. Lenge, M., A. Ramalli, P. Tortoli, C. Cachard, and H. Liebgott. Plane-wave transverse oscillation for high-frame-rate 2-d vector flow imaging. *IEEE Transactions on Ultrasonics, Ferroelectrics, and Frequency Control*. 62(12):2126–2137, 2015.
30. Jensen, J., C. A. V. Hoyos, M. B. Stuart, C. Ewertsen, M. B. Nielsen, and J. A. Jensen. Fast plane wave 2-d vector flow imaging using transverse oscillation and directional beamforming. *IEEE*

Transactions on Ultrasonics, Ferroelectrics, and Frequency Control. 64(7):1050–1062, 2017.

31. Jensen, J., M. B. Stuart, J. A. Jensen, and High frame rate vector velocity estimation using plane waves and transverse oscillation. In *IEEE International Ultrasonics Symposium (IUS)*. IEEE, pp. 1–4, 2015.
32. Ricci, S., A. Ramalli, L. Bassi, E. Boni, and P. Tortoli. Real-time blood velocity vector measurement over a 2-d region. *IEEE Transactions on Ultrasonics, Ferroelectrics, and Frequency Control*. 65(2):201–209, 2017.
33. Wang, I.-C., H. Huang, W.-T. Chang, and C.-C. Huang. Wall shear stress mapping for human femoral artery based on ultrafast ultrasound vector doppler estimations. *Medical Physics*. 48(11):6755–6764, 2021.
34. Chee, A. J., Ho, C. K., Yiu, B. Y., Alfred, C. Time-resolved wall shear rate mapping using high-frame-rate ultrasound imaging. *IEEE Transactions on Ultrasonics, Ferroelectrics, and Frequency Control*. 2022.
35. Du, Y., A. Goddi, C. Bortolotto, Y. Shen, A. Dell'Era, F. Calliada, and L. Zhu. Wall shear stress measurements based on ultrasound vector flow imaging: theoretical studies and clinical examples. *Journal of Ultrasound in Medicine*. 39(8):1649–1664, 2020.
36. Leow, C. H., and M.-X. Tang. Spatio-temporal flow and wall shear stress mapping based on incoherent ensemble-correlation of ultrafast contrast enhanced ultrasound images. *Ultrasound in Medicine & Biology*. 44(1):134–152, 2018.
37. Ramalli, A., K. Aizawa, A. C. Shore, C. Morizzo, C. Palombo, M. Lenge, and P. Tortoli. Continuous simultaneous recording of brachial artery distension and wall shear rate: a new boost for flow-mediated vasodilation. *IEEE Transactions on Ultrasonics, Ferroelectrics, and Frequency Control*. 66(3):463–471, 2018.
38. Poelma, C., R. Van Der Mijle, J.-M. Mari, M.-X. Tang, P. D. Weinberg, and J. Westerweel. Ultrasound imaging velocimetry: toward reliable wall shear stress measurements. *European Journal of Mechanics-B/Fluids*. 35:70–75, 2012.
39. Riemer, K., E. M. Rowland, J. Broughton-Venner, C. H. Leow, M. Tang, and P. Weinberg. Contrast agent-free assessment of blood flow and wall shear stress in the rabbit aorta using ultrasound image velocimetry. *Ultrasound in Medicine & Biology*. 48(3):437–449, 2022.
40. Riemer, K., E. Rowland, C. Leow, M. Tang, and P. Weinberg. Determining haemodynamic wall shear stress in the rabbit aorta in vivo using contrast-enhanced ultrasound image velocimetry. *Annals of Biomedical Engineering*. 48(6):1728–1739, 2020.
41. Kim, H.-B., J. Hertzberg, C. Lanning, and R. Shandas. Noninvasive measurement of steady and pulsating velocity profiles and shear rates in arteries using echo PIV: in vitro validation studies. *Annals of Biomedical Engineering*. 32:1067–1076, 2004.
42. Kim, S., Jing, B., Lane, B., Padala, M., Veneziani, A., Lindsey, B. Dynamic coronary blood flow velocity and wall shear stress estimation using ultrasound in an ex vivo porcine heart to appear. *Cardiovascular Engineering and Technology*. 2024.
43. Dodge, J. T., Jr., B. G. Brown, E. L. Bolson, and H. T. Dodge. Lumen diameter of normal human coronary arteries influence of age, sex, anatomic variation, and left ventricular hypertrophy or dilation. *Circulation*. 86(1):232–246, 1992.
44. Zhang, J.-M., L. Zhong, T. Luo, Y. Huo, S. Y. Tan, A. S. L. Wong, B. Su, M. Wan, X. Zhao, G. S. Kassab, et al. Numerical simulation and clinical implications of stenosis in coronary blood flow. *BioMed Research International*. 2014.
45. Tonino, P. A., W. F. Fearon, B. De Bruyne, K. G. Oldroyd, M. A. Leesar, P. N. Ver Lee, P. A. MacCarthy, M. Van't Veer, and N. H. Pijls. Angiographic versus functional severity of coronary artery stenoses in the fame study: fractional flow reserve versus angiography in multivessel evaluation. *Journal of the American College of Cardiology*. 55(25):2816–2821, 2010.
46. De Bruyne, B., W. F. Fearon, N. H. Pijls, E. Barbato, P. Tonino, Z. Piroth, N. Jagic, S. Mobius-Winckler, G. Rioufol, N. Witt, et al. Fractional flow reserve-guided PCI for stable coronary artery disease. *New England Journal of Medicine*. 371(13):1208–1217, 2014.
47. SolidWorks, D. S. Solidworks®. *Version Solidworks*.1, 2005.
48. Madsen, E. L., J. A. Zagzebski, R. A. Banjavie, and R. E. Jutila. Tissue mimicking materials for ultrasound phantoms. *Medical Physics*. 5(5):391–394, 1978.
49. Hozumi, T., K. Yoshida, T. Akasaka, Y. Asami, Y. Ogata, T. Takagi, S. Kaji, T. Kawamoto, Y. Ueda, and S. Morioka. Noninvasive assessment of coronary flow velocity and coronary flow velocity reserve in the left anterior descending coronary artery by doppler echocardiography: comparison with invasive technique. *Journal of the American College of Cardiology*. 32(5):1251–1259, 1998.
50. Sharif, D., A. Sharif-Rasslan, C. Shahla, A. Khalil, and U. Rosenschein. Differences in coronary artery blood velocities in the setting of normal coronary angiography and normal stress echocardiography. *Heart International*. 10(1):5000221, 2015.
51. Inc., T.M.: MATLAB Version: 9.12.0 (2022). https://www.mathworks.com
52. Demené, C., T. Deffieux, M. Pernot, B.-F. Osmanski, V. Biran, J.-L. Gennisson, L.-A. Sieu, A. Bergel, S. Franqui, J.-M. Correas, et al. Spatiotemporal clutter filtering of ultrafast ultrasound data highly increases doppler and fultrasound sensitivity. *IEEE Transactions on Medical Imaging*. 34(11):2271–2285, 2015.
53. Pihl, M. J., and J. A. Jensen. A transverse oscillation approach for estimation of three-dimensional velocity vectors, part I: concept and simulation study. *IEEE Transactions on Ultrasonics, Ferroelectrics, and Frequency Control*. 61(10):1599–1607, 2014.
54. Lankton, S. Sparse field methods-technical report. Georgia Institute of Technology, 2009.
55. Kim, S., B. Jing, A. Veneziani, and B. D. Lindsey. Blood flow velocity and wall shear stress estimation in forward-viewing intravascular ultrasound imaging: comparison of doppler and particle image velocimetry (PIV) approaches. In: IEEE International Ultrasonics Symposium (IUS). IEEE, 2021, pp. 1–4.
56. Formaggia, L., A. Quarteroni, and A. Veneziani. Cardiovascular Mathematics: Modeling and Simulation of the Circulatory System, Vol. 1, Milan: Springer, 2010.
57. Cleveland, W. S., and S. J. Devlin. Locally weighted regression: an approach to regression analysis by local fitting. *Journal of the American Statistical Association*. 83(403):596–610, 1988.
58. Quarteroni, A., R. Sacco, and F. Saleri. Numerical Mathematics, Vol. 37, Berlin Heidelberg: Springer, 2010.
59. Vretblad, A. Fourier Analysis and Its Applications, Vol. 223, New York: Springer, 2003.
60. Langtangen, H. P., and A. Logg. Solving PDEs in Python: The FEniCS Tutorial I. Berlin Heidelberg: Springer, 2017.
61. Ern, A., and J.-L. Guermond. Theory and Practice of Finite Elements, Vol. 159, Berlin Heidelberg: Springer, 2004.
62. Brands, P. J., A. P. Hoeks, L. Hofstra, and R. S. Reneman. A noninvasive method to estimate wall shear rate using ultrasound. *Ultrasound in Medicine & Biology*. 21(2):171–185, 1995.
63. Boyd, J. P. Chebyshev and Fourier Spectral Methods. New York: Courier Corporation, 2001.